Incorporation of Sb^{5+} into CeO_2: Local Structural Distortion of the Fluorite Structure From a Pentavalent Substituent

Craig I. Hiley,[1] Janet M. Fisher,[2] Reza J. Kashtiban,[3] Giannantonio Cibin,[4] David Thompsett[2] and Richard I. Walton[1]*

1. Department of Chemistry, University of Warwick, Gibbet Hill Road, Coventry, CV4 7AL, UK*Author for correspondence: r.i.walton@warwick.ac.uk

2. Johnson Matthey Technology Centre, Blounts Court, Sonning Common, Reading, RG4 9NH, UK

3. Department of Physics, University of Warwick, Gibbet Hill Road, Coventry CV4 7AL, UK

4. Diamond Light Source Ltd, Harwell Science and Innovation Campus, Didcot, OX11 0DE, UK

Abstract Hydrothermal crystallisation of CeO_2 from aqueous sodium hydroxide solution at 240 °C using $CeCl_3 \cdot 7H_2O$ in the presence of hydrogen peroxide with addition of either $SbCl_3$ or $SbCl_5$ yields polycrystalline samples of antimony-containing ceria directly from solution. Powder X-ray diffraction sShows a contraction of the cubic lattice parameter with increasing Sb content, and also a broadening of Bragg peaks, from which Scherrer analysis yields crystallite domain sizes of 5 - 20 nm. Scanning transmission electron microscopy provides consistent results with observation of highly crystalline particles of a few nm in diameter. X-ay absorption near edge structure spectroscopy at the Ce L_{III} and Sb K edges reveals the presence of Ce^{4+} and Sb^{5+} in the solids. To balance charge the presence of co-included Na is proposed, corroborated by elemental analysis. The general chemical formula of the materials can thus be written as $(Ce_{1-x}Sb_x)_{1-y}Na_yO_{2-\delta}$ (where $x < 0.4$ and $y \geq x/3$). Sb K-edge extended X-ray absorption fine structure spectroscopy of the substituted ceria samples shows that the local structure of Sb resembles that in $NaSbO_3$, where six-coordinate metal sites are found, but with evidence of a longer interatomic correlation due to surrounding Ce/Sb atoms in the fluorite structure; this implies that the Sb is displaced from the ideal eight-coordinate site of the fluorite structure. This structural distortion gives materials that are unstable under reducing conditions, coupled by the ease of reduction to elemental antimony, which is extruded leading to phase separation.

Table of Contents Entry

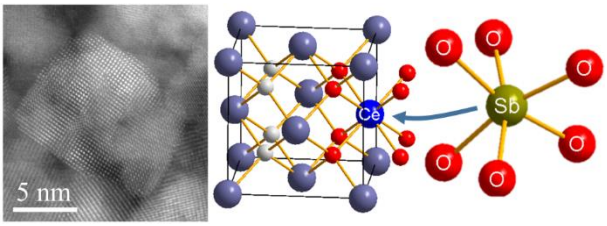

Sb^{5+}-substituted CeO_2 crystallises directly from solution: the substituent cation has octahedral coordination, implying local structural distortion of the fluorite structure.

Introduction

Cerium dioxide, ceria, is well known for its considerable uses in heterogeneous catalysis where it provides a redox-active support material, often for precious metals, that allows storage and release of oxygen.[1] These properties arise from the reversible switching of cerium oxidation state from +4 to +3, aided by oxide ion transport in the fluorite lattice. The use of ceria as one of the components in three-way automotive catalytic convertors dates back to the 1970s, and this relies on its inherent oxygen storage capacity providing oxygen under fuel rich conditions and promoting reduction when the exhaust is lean.[2] Other more recent applications of ceria in catalyst supports include in diesel soot oxidation,[3] CO oxidation, such as in the water-gas-shift reaction used for removal of carbon monoxide from hydrogen streams produced by steam reforming,[4] and in the oxidation of volatile organic compounds.[5] More widely, ceria has been reported as a functional solid in diverse areas, such as UV shielding in cosmetics,[6] humidity sensing,[7] antimicrobial activity,[8] solar splitting of water and carbon dioxide,[9] and is used as an abrasive.[10] Emerging work on ceria materials is focussing on using nanostructure to tune properties, with emphasis upon uses in environmental fields.[11]

An important strategy in optimising the properties of ceria for any of its uses is the partial substitution of cerium by another element whilst maintaining the average fluorite structure. The case of ceria-zirconia is especially well-developed in this respect and over a wide composition range Ce^{4+} can be replaced by Zr^{4+} to yield a ternary oxide system, with certain compositions having cation-ordered configurations under specific preparative conditions.[12] In ceria-zirconias the bulk oxygen content is stoichiometric since the cation substitution is isovalent, but the effect of the cation size mismatch is to induce local strain and it is this that is believed to be responsible for enhanced oxygen storage capacity.[13] If an aliovalent substituent is introduced into ceria then charge must be balanced by oxygen non-stoichiometry; commonly +3 cations are used and often lanthanide ions, since their radius is similar to Ce^{4+} and so have a preference for high coordination numbers appropriate for the fluorite structure. The case of Gd^{3+}-substituted ceria is especially well-studied since the material finds application as a solid-oxide conductor, such as an anode in solid-oxide fuel cells;[14] here, the presence of charge-balancing oxide-ion vacancies provides hopping pathways for ionic conduction. In fact ceria is remarkably accommodating in terms of the substituent species that can be taken up and elements from all parts of the Periodic Table have been reported as substituting for cerium in its structure.[15] This includes transition-metals such as Fe[16] and Ti[17], s-block cations, such as Ca[18] and Na[19] and main-group elements such

as In[20] and Pb.[21] Each substituent element brings its own coordination preference and distinctive chemistry to the material that may be beneficial for catalytic applications.

Solution-mediated crystallisation provides a versatile route to oxide materials, and hydrothermal chemistry in particular has been developed to allow formation of atomically homogeneous multi-element oxides under mild conditions.[15, 22] From this work it is evident that unusual substitutional chemistry can be achieved, with high levels of incorporation of particular elements or inclusion of ions with considerable size mismatch that would not be possible at high temperatures, where phase separation would occur. In the case of hydrothermal synthesis of ceria[23] our own work has demonstrated the crystallisation of Pd^{2+}-containing CeO_2, with the substituent occupying interstitial square-planar sites and expanding the fluorite lattice,[24] while inclusion of Bi^{3+} can be achieved to a higher degree in hydrothermal reactions than by conventional solid-state synthesis, giving a significant expansion of the unit cell.[25]

We recently reported the hydrothermal formation of Nb^{5+}-containing ceria and showed how the unusually highly-charged substituent could be accommodated in the fluorite structure by a displacement from the ideal 8-coordinate cation site, in turn leaving under-coordinated oxide ions that account for the observed enhanced oxygen storage capacity of the material.[26] The element niobium is unique in possessing a stable +5 oxidation state that is not easily reduced and charge balance in CeO_2 is achieved by co-inclusion of Na^+ from the alkali solution used in its synthesis. To explore further the counterintuitive idea of using a pentavalent substituent to disrupt the local structure of ceria, we herein report a study of inclusion of the element antimony. Like niobium, antimony also has an accessible +5 oxidation state, although reduction to the +3 oxidation state can more readily occur; the incorporation of antimony into ceria has not to our knowledge been previously reported.

Results and Discussion

Figures 1a and 1c show profile fits to powder X-ray diffraction (XRD) patterns, and Figures 1b and 1d show lattice parameters and crystallite domain sizes determined by profile fitting against these patterns from samples prepared using either $SbCl_5$ or $SbCl_3$ as an antimony source with the ratio of metal salts used in synthesis defined as (1-x)Ce: xSb. Similar trends are seen in each case with a contraction of the lattice with increasing Sb added in synthesis, which is consistent with the smaller ionic radii of both Sb^{3+} and Sb^{5+} (in six-coordinate sites) compared to the eight-coordinate Ce^{4+} in ceria.[27] The fact that the lattice

parameter decreases with increasing x with the same gradient, however, would suggest the same oxidation state of antimony is found in both sets of materials (see below for spectroscopic confirmation of this). The crystallite domain sizes derived from Scherrer analysis of the peak broadening in the XRD profile show a decrease with increasing Sb content. This effect has been seen in other hydrothermally prepared ceria samples with increasing substituent level.[24-26] Whilst the crystallite domain sizes of the samples prepared using $SbCl_5$ decrease approximately linearly (Figure 1b), the crystallite size drops abruptly upon addition of even a small amount of antimony (x = 0.05) in samples prepared using $SbCl_3$, which is then followed by a modest decrease in crystallite size over the range $0 \leq x \leq 0.35$.(Figure 1d). The contrasting behaviour must be a result of the different solution chemistry taking place, such as the different concentration of chloride used in the synthesis or the differing redox chemistry possible with the different antimony oxidation states. Ultimately, however, a similar crystallite domain size of ~5 nm is reached for both sets of samples at the highest amount of antimony included, x = 0.4 for materials prepared from $SbCl_5$ and x = 0.35 for materials prepared from $SbCl_3$.

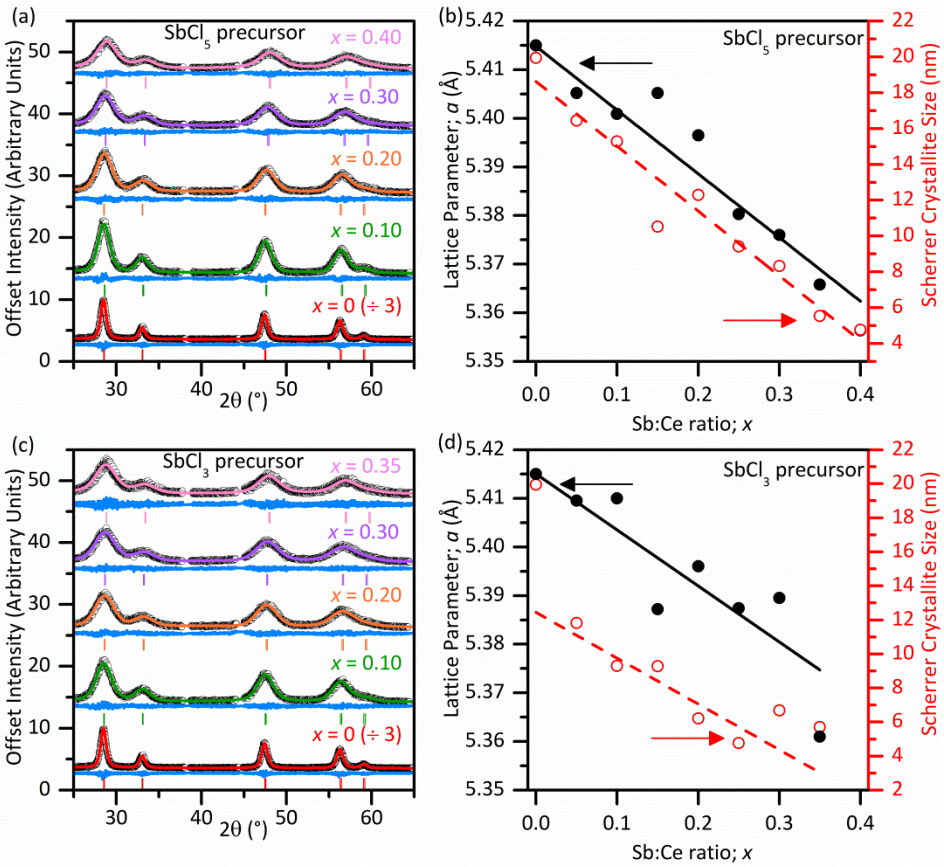

Figure 1: Powder XRD (λ = 1.5418 Å) analysis of Sb-substituted ceria materials: left, fitted profiles and, right, refined cubic lattice parameters and Scherrer crystallite size for (a-b) materials prepared from $SbCl_5$ and (c-d) materials prepared from $SbCl_3$. In (a,c) the difference lines are shown in blue under the fitted profile, and the excluded regions at ~38° 2θ and ~44° 2θ are due to the sample holder.

The particle size as visualised by transmission electron microscopy (TEM), Figure 2, shows consistent results, with the powder XRD analysis with crystallites of a few nanometres in size observed for the Sb-substituted materials. The samples consist of agglomerated particles, but a high level of crystallinity is evident in the high-resolution images since lattice fringes are apparent even in the smallest crystallites. The particle size is notably smaller for the Sb-containing materials compared to the CeO_2 prepared using the same hydrothermal method, and furthermore the particle size is smaller for samples that contain a higher level of Sb, consistent with the Scherrer analysis of powder XRD.

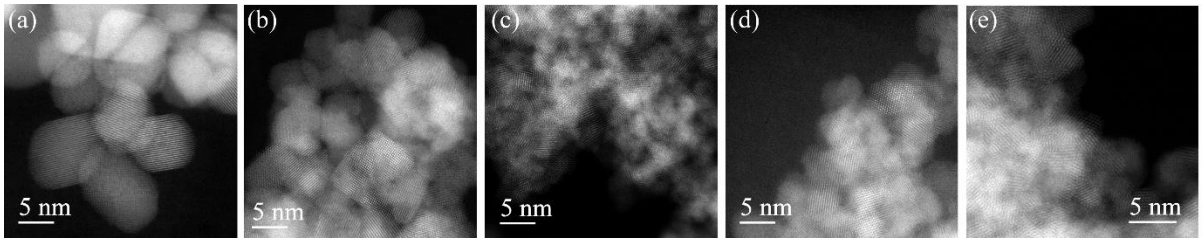

Figure 2: Scanning TEM micrographs from Sb-substituted ceria materials (a) x = 0, (b) x = 0.05 and (c) x = 0.30 prepared using $SbCl_5$ precursor, (d) x = 0.05 and (e) x = 0.30 prepared using $SbCl_3$ precursor.

TEM was also used to examine the distribution of Sb in the specimens using energy-dispersive X-ray analysis (EDXA) mapping, Figure 3. These show the presence of antimony throughout the crystallites with no evidence for clustering of the elements on the tens of nanometre scale.

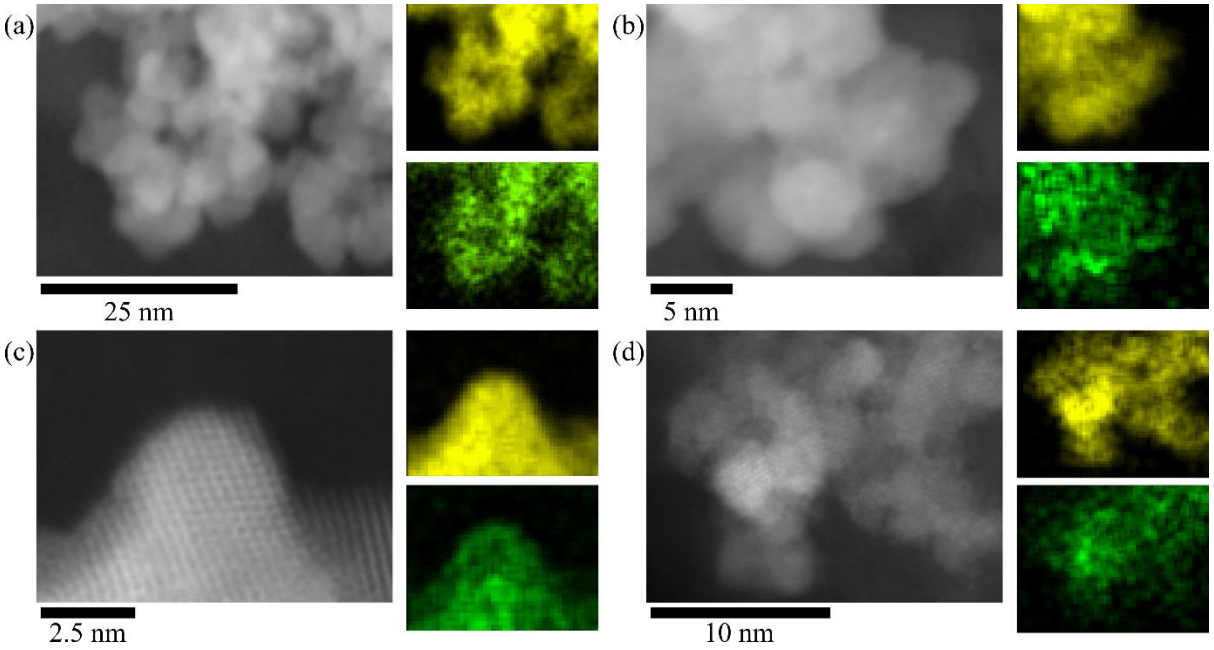

Figure 3: EDXA maps showing Ce L signal in yellow and Sb signal L in green recorded using TEM from the regions show in the micrographs to the left: (a) x = 0.05 prepared using $SbCl_5$ precursor (b) x = 0.05 prepared using $SbCl_3$ precursor, (c) x = 0.30 prepared using $SbCl_5$ precursor and (d) x = 0.30 prepared using $SbCl_3$ precursor.

Raman spectra of each of the materials show a broad band centred at around 459 – 465 cm^{-1} (Figure 4), attributed to the F_{2g} Raman mode caused by M – O symmetric stretching in an MO_8 cube, the characteristic stretch in fluorite oxides.[28] This band broadens as Sb content increases, indicative of increasing disorder. As Sb content increases a second band begins to appear ~600 cm^{-1}, which is commonly assigned as a phonon mode arising from oxide vacancies.[16, 29] There are no other observed Raman bands, confirming that no other phases are present.

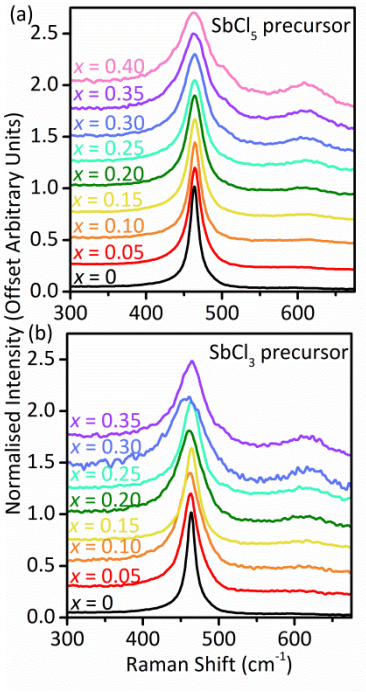

Figure 4: Raman spectra of Sb-substituted ceria materials synthesised using (a) $SbCl_5$ and (b) $SbCl_3$ as the precursor.

X-ray absorption near-edge structure (XANES) spectroscopy measured at the Ce L_{III}-edge and the Sb K-edge was used to determine the bulk average oxidation state of the elements in the two sets of samples studied, Figure 5. This clearly shows how cerium maintains its oxidation state of +4 as in CeO_2 but also that antimony is found in the +5 oxidation state irrespective of the Sb oxidation state in the precursor materials, which can be explained by the oxidising conditions in the hydrothermal reaction mixture provided by hydrogen peroxide.

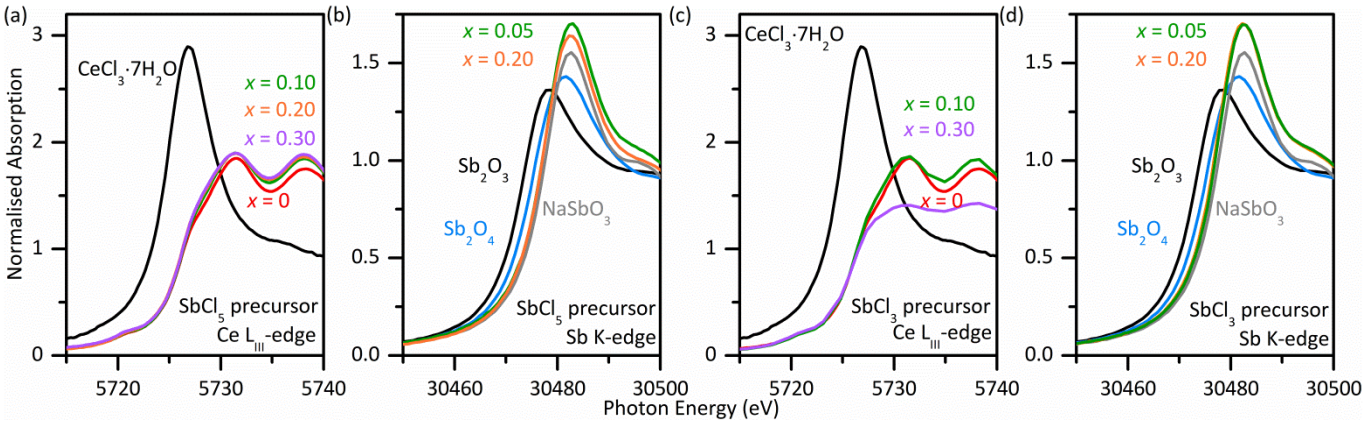

Figure 5: Ce L_{III}-edge (a,c) and Sb K-edge (b, d) XANES of Sb-substituted ceria samples synthesised using (a,b) $SbCl_5$ and (c,d) $SbCl_3$ as the precursor. In (c) the spectrum of the x

= 0.3 sample is affected by high absorptivity of the specimen but the XANES is nevertheless characteristic of Ce(IV).

The mechanism of charge-balance needs to be considered, with the presence of a pentavalent substituent requiring a different mechanism than the commonly used lower-valent substituents in ceria (trivalent or divalent cations). Oxide excess in fluorite oxides is possible, such as in the mixed-valent uranium oxides $UO_{2+\delta}$ where extra oxide is present in interstitial sites to allow oxidation of a fraction of the uranium to the +5 oxidation state.[30] Another possibility for the Sb^{5+}-substituted materials would be the presence of some Ce^{3+} to maintain charge neutrality, but this is ruled out by the XANES spectroscopy results. In the case of Nb^{5+} inclusion, which we recently reported,[26] we found that charge balance was possible by co-inclusion of Na^{+}, provided by the alkali solution used in synthesis: for every three Nb (or Sb) substituted into the structure one Ce could be substituted by a Na, or in Kröger-Vink notation:

$$4Ce_{Ce}^{\times} \Rightarrow 3Sb_{Ce}^{\bullet} + Na_{Ce}^{\prime\prime\prime}$$

The presence of sodium in the Sb-containing materials was proven by inductively coupled plasma atomic emission spectroscopy (ICP-OES) analysis on samples that had been washed in boiling water, and this shows that at least 1 Na is present for each 3Sb, Figure 6, consistent with a similar charge-balancing mechanism as for the Nb materials.[26] In fact, as for Nb-substituted ceria it is typically found that slightly more than the required amount of sodium was included in the materials, implying in turn some oxide vacancies. This would be consistent with the Raman spectra reported above that suggests the presence of oxide defects, and therefore we can propose a general chemical formula of the new materials as $(Ce_{1-x}Sb_x)_{1-y}Na_yO_{2-\delta}$ (where $x < 0.4$ and $y \geq x/3$).

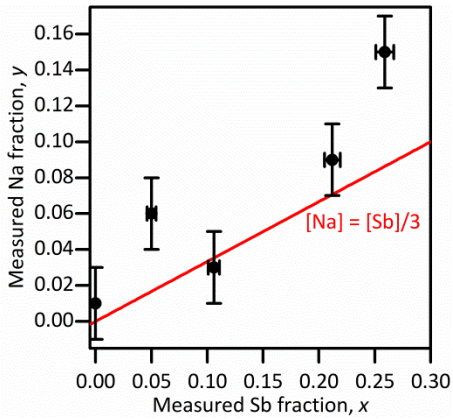

Figure 6: Elemental analysis results from Sb-substituted ceria prepared from $SbCl_5$ showing how the amount of sodium is at least 1/3 of the amount of Sb measured, implying charge-balance by inclusion of Na^+.

The presence of Sb^{5+} in an average fluorite lattice would imply a local structural distortion since the substituent has a distinct preference for octahedral coordination (albeit distorted), such as in $NaSbO_3$ with either the ilmenite structure or the perovskite structure at high pressure[31] and in $KSbO_3$ with a cubic, tunnel structure.[32] To examine the environment of antimony in our materials we analysed Sb K-edge extended X-ray absorption fine structure (EXAFS) spectra, using $NaSbO_3$ and orthorhombic Sb_2O_3 (valentinite)[33] as reference materials for comparison. Figure 7 shows the fitted EXAFS spectra and their Fourier transforms of representative samples (see ESI for all spectra) and Tables 1 and 2 show the fitted structural parameters for the reference materials and the ceria samples, respectively. In this analysis the amplitude reduction factor, S_0^2, was refined for the reference materials giving a value close to 1 (1.1 ± 0.1), as expected, and then for the substituted ceria materials it was fixed at that value. It can be seen that the refined Sb-O distances in all of the substituted ceria materials is close to the value seen in $NaSbO_3$ and with a similar Debye-Waller factor at room temperature when the coordination number is set at 6. In contrast, in Sb_2O_3 the antimony is found in irregular coordination with 3 short and 2 long Sb-O distances.[33] Thus the EXAFS analysis confirms the presence of Sb^{5+} in six-coordinate sites, close to octahedral as in $NaSbO_3$. The data also provide evidence for a longer interatomic correlation at around 3.7 Å in the substituted ceria materials, not seen in $NaSbO_3$. Assuming that the Sb resides close to the cubic metal site in the fluorite lattice then one would expected 12 surrounding other Ce atoms 3.84 Å in the face-centred cubic lattice[34] (and some of these statistically would be Sb atoms which may be obvious at higher levels of substitution). We thus modelled the longer interatomic distance as shells of cerium and antimony atoms, 12 in total, with the relative amount set at the values expected from the composition, Table 2. This gave a statistically improved fit to the spectra with physically reasonable refined parameters. Further analysis of selected samples revealed corroborative evidence for the correct assignment of this feature: for three materials prepared from $SbCl_3$ with 10 %, 20 % and 30 % of the cerium replaced by antimony, the refined distance of the Sb/Ce shell systematically decreases with increasing Sb content, despite the invariant Sb-O distance, Table 1. This is entirely consistent with the contraction of lattice parameter seen by powder XRD with addition of increasing amounts of Sb.

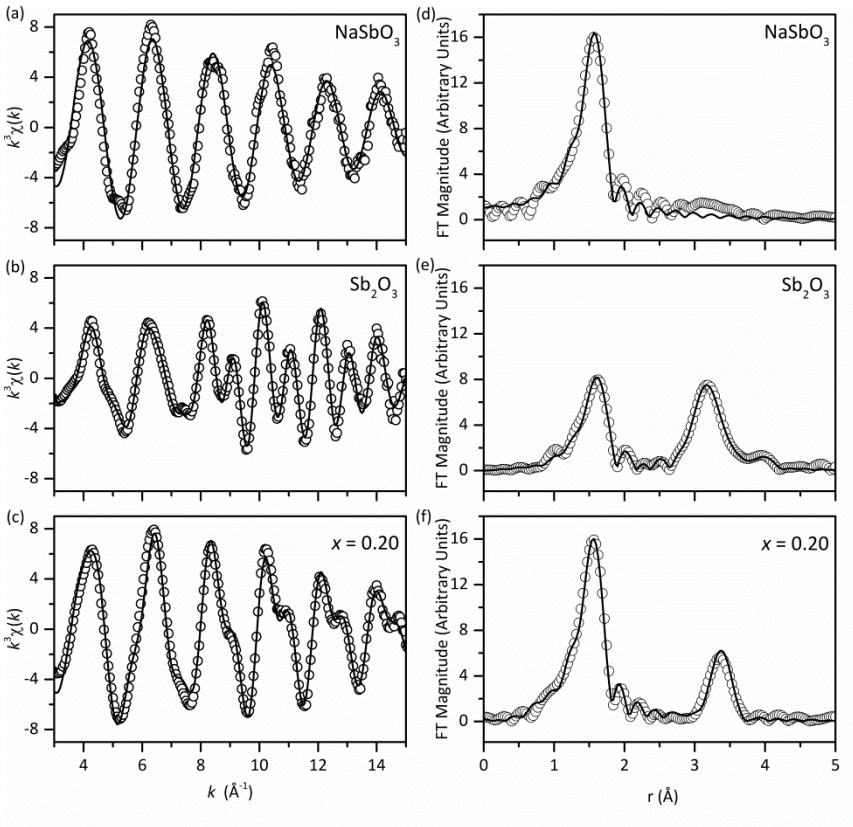

Figure 7: Sb K-edge EXAFS (left) and their corresponding Fourier Transforms (right) of (a,d) $NaSbO_3$ (298 K), (b,e) Sb_2O_3 (valentinite, 77 K) and (c,f) Sb-substituted ceria with x = 0.20 prepared from $SbCl_3$ (77 K). Points are measured data and the full line the fitted curve (see Tables 1 and 2 for fitted parameters).

Table 1: Fitted EXAFS parameters from crystalline reference materials. *N*, the coordination number was fixed at the expected value and the radial distance, *R* and Debye-Waller factor σ^2, were varied in least-squares refinements. R_{cryst} is the expected crystallographic distance (see text), S_0^2 the amplitude reduction factor and E_0 the threshold energy.

Material	**Shell**	***N***	***R*/Å**	R_{cryst}**/Å**	σ^2**/Å^2**	S_0^2	E_0**/eV**	**R-factor**
$NaSbO_3$	O	6	1.980(7)	1.973	0.0031(6)	1.1(1)	4.9	0.050
Sb_2O_3	O	3	2.008(6)	2.006	0.0036(7)	1.1(1)	8.5	0.024
	O	2	2.523(48)	2.569	0.0165(86)			
	Sb	2	3.397(6)	3.393	0.0035(5)			
	Sb	2	3.699(14)	3.709	0.0060(14)			
	Sb	2	3.988(4)	3.940	0.0102(35)			
	Sb	4	4.130(23)	4.085	0.0061(22)			

Table 2: Fitted EXAFS parameters from Sb-substituted ceria samples. For definition of parameters, see Table 1. The amplitude reduction factor was fixed at the value obtained for the reference materials (see text).

Material	**Temperature / K**	**Shell**	***N***	***R*/Å**	**σ^2/Å^2**	***E*$_0$/eV**	**R-factor**
x = 0.40 from $SbCl_5$	77	O	6	1.970(5)	0.0032(4)	1.8	0.077
		Ce	7.2	3.642(98)	0.0096(7)		
		Sb	4.8				
x = 0.40 from $SbCl_5$	298	O	6	1.971(7)	0.0037(5)	2.9	0.082
		Ce	7.2	3.644(39)	0.0111(12)		
		Sb	4.8				
x = 0.30 from $SbCl_3$	298	O	6	1.971(7)	0.0040(5)	2.8	0.068
		Ce	8.4	3.660(24)	0.0148(24)		
		Sb	3.6				
x = 0.20 from $SbCl_3$	298	O	6	1.970(7)	0.0035(5)	2.5	0.087
		Ce	9.6	3.666(28)	0.0157(29)		
		Sb	2.4				
x = 0.10 from $SbCl_3$	298	O	6	1.973(10)	0.0043(7)	2.5	0.090
		Ce	10.8	3.679(54)	0.0206(68)		
		Sb	1.2				

Temperature programmed reduction (TPR) is one of the common tests for the redox properties of ceria materials.[35] We selected one of the Sb-substituted cerias, with the lowest Sb content (x = 0.05) prepared from $SbCl_5$, to measure hydrogen TPR and compared the result with a pure ceria sample prepared by the same hydrothermal method, Figure 8a. Note that heating in H_2 to temperatures beyond 550 °C was not performed due to the possibility of releasing toxic Sb (a volatile solid with a melting point of 631 °C) or even SbH_3, a highly poisonous gas. The pure ceria sample shows behaviour similar to high surface area materials reported in the literature with a low-temperature reduction with a maximum uptake around 300 °C, due to reduction of the surface of the crystallites, followed by the onset of a higher temperature reduction beginning above 500 °C due to the bulk reduction of the fluorite lattice. The x =0.05 sample shows a completely different TPR profile, with the absence of the low temperature surface reduction and instead much larger reduction feature at around 400 °C. The process was mimicked *ex situ* using a sample with higher Sb content so to detect the decomposition product, and powder XRD revealed that the reduction yielded a mixture of CeO_2 and elemental Sb, Figure 8b. The lattice parameter of the ceria material before (5.4061(6) Å) and after (5.4161(4) Å) reduction confirms the extrusion of Sb from the structure with a corresponding increase in lattice parameter. Quantification of the amount of hydrogen oxidised in TPR experiments is equivalent (within error) to the amount required to reduce Sb^{5+} to Sb metal, suggesting that little Ce reduction takes place below 550 °C. Similar behavious has previously been found for Bi-substituted ceria, where the extrusion of Bi occurs under strongly reductive conditions. However, in that case the heavier Group 15 substituent was found in the +3 oxidation state, reflecting the relative instability of the highest oxidation state of bismuth compared to antimony studied here.[25]

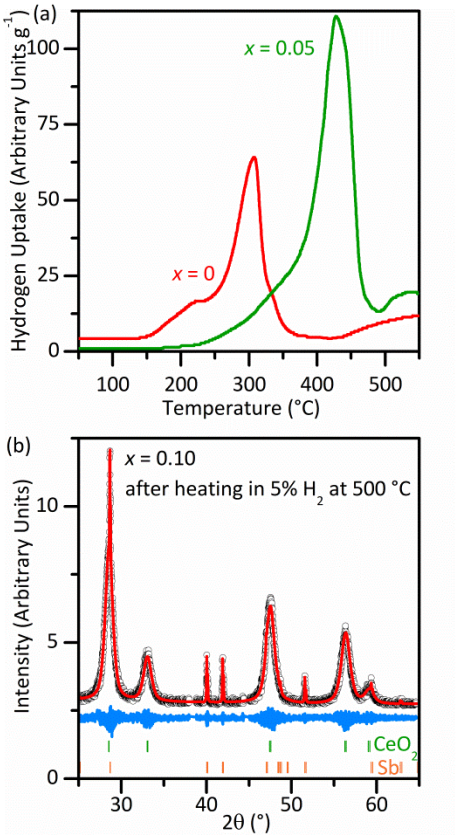

Figure 8: (a) Temperature programmed reduction and (b) powder XRD after heating of Sb-substituted ceria.

Conclusions

Antimony can be introduced into the cubic fluorite structure of CeO_2 by hydrothermal synthesis with up to 40 % of the cerium replaced by Sb^{5+}. Charge-balance is maintained by co-inclusion of Na^+ from the reaction medium, rather than by reduction of the Ce^{4+}, in the same mechanism as we previously found for niobium-substituted ceria. The presence of these pentavalent substituents, with their preference for lower coordination numbers than cerium, gives rise to local distortion of the fluorite structure. In the case of antimony, and in contrast to niobium, this gives materials that are unstable to heating under reducing conditions, most likely aided by the ease of reduction to the elemental state of the substituent. This shows how the hydrothermal synthesis method provides access to substituted oxides that would be difficult, or impossible to prepare using high temperature calcination or annealing. While the antimony-substituted ceria is inherently unstable under strongly reducing conditions, its reactivity may be useful for many of the other catalysis applications that ceria is studied for, and the investigation of this chemistry will be the focus of ongoing work.

Experimental

6 mmol total of $CeCl_3 \cdot 7H_2O$ and either $SbCl_5$ or $SbCl_3$ in the required ratio (1-x)Ce : xSb was dissolved in 2 ml distilled water, followed by the addition of 2 ml of H_2O_2 (37% aqueous solution). This solution was then stirred for 15 minutes, during which the colour of the solution changed from colourless to a pale yellow/orange colour, indicating Ce^{3+} oxidation to Ce^{4+}. Next, 8 ml of either 7.5 mol dm^{-3} NaOH was added dropwise, giving effervescence. The red-brown gel was stirred for a further 10-15 minutes before being sealed in a Teflon-lined steel autoclave and heated in a fan oven to 240 °C for 24 hours. The autoclave was cooled to room temperature before filtration and washing with copious amounts of boiling water. The resulting brown solids were dried in an oven at 80 °C overnight and ground in a pestle and mortar to give a fine powder. Sb_2O_4 was prepared by heating Sb_2O_3 in air to 500 °C, while the reference materials $NaSbO_3$ and Sb_2O_3 were used as purchased from Alfa Aesar; their identity was confirmed by powder XRD.

Powder XRD were measured using a Siemens D5000 diffractometer in Bragg-Brentano mode operating with Cu $K\alpha_{1/2}$ radiation and the diffraction profiles were fitted using the Le Bail method using the software GSAS[36] implemented with EXPGUI.[37] Scherrer analysis was performed by subtracting a contribution to instrumental broadening, determined using a NIST ceria reference.

Scanning transmission electron microscopy (STEM) analysis was carried out on a doubly corrected JEOL ARM200F microscope operating at 200 kV. Annular darkfield STEM (ADF-STEM) images were obtained using a JEOL annular field detector at a probe current of ~23 pA with a convergence semiangle of ~25 mrad. EDXA measurements were carried out with an Oxford Instrument X-Max^N 100TLE windowless SDD to determine the elemental composition and distribution.

X-ray absorption spectroscopy was performed on beamline B18 of the Diamond Light Source, UK.[38] Data were collected from samples diluted with appropriate amounts of polyethylene powder and pressed in self-supporting discs around 1 mm thick in transmission mode at the Ce L_{III}-edge and the Sb K-edges. Incident energies were selected using a water-cooled, fixed-exit, double-crystal monochromator with either Si(111) or Si(311) crystals for the Ce L_{III} and Sb K edges, respectively. The beam was focussed horizontally and vertically

using a double toroidal mirror, coated with Pt, 25 m from the source, while a pair of smaller plane mirrors were used for harmonic rejection. The raw data were normalised using the software ATHENA[39] to produce XANES spectra and EXAFS spectra for modelling using the software ARTEMIS.[39] The k^3-weighted Sb K-edge EXAFS spectra were analysed over the *k*-range 3 – 15.9 $Å^{-1}$ with the amplitude reduction factor determined from the reference materials $NaSbO_3$ and Sb_2O_3 used for the analysis of the Sb-substituted cerias.

Raman spectra were recorded from solid samples using a Bruker MultiRAM spectrometer operating with a Nd:YAG laser (1064 nm) with 4 cm^{-1} resolution and 200 mW incident beam.

Analysis of metals in the samples was performed using inductively coupled plasma-optical emission spectroscopy (ICP-OES) after digestion of the samples in hydrobromic acid.

Temperature-programmed reduction (TPR) was performed at the Johnson Matthey Technology Centre using 10% H_2 in N_2. H_2 consumption was measured by the variation in thermal conductivity of the gas before and after contact with the sample with a water trap after the sample to absorb water created by H_2 oxidation. In order to quantify accurately the hydrogen consumption a known quantity (1 ml) of N_2 was injected into the H_2/N_2 gas stream before the experiment began to create a calibration peak.

Acknowledgements

CIH was funded by an EPSRC industrial CASE studentship and we thank Johnson Matthey plc for their financial contribution to this award. Some of the equipment used in materials characterisation at the University of Warwick was obtained through the Science City Advanced Materials project "Creating and Characterising Next Generation Advanced Materials" with support from Advantage West Midlands (AWM) and part funded by the European Regional Development Fund (ERDF). We are grateful to Diamond Light Source Ltd for provision of beamtime (references SP5828 and SP7253).

References

1. (a) R. J. Gorte, *AlChE J.*, 2010, **56**, 1126-1135; (b) A. Trovarelli and P. Fornasiero, *Catalysis by Ceria and Related Materials, 2nd Edition* Imperial College Press, London, 2013; (c) T. Montini, M. Melchionna, M. Monai and P. Fornasiero, *Chem. Rev.*, 2016, **116**, 5987-6041.
2. R. Di Monte and J. Kašpar, *Top. Catal.*, 2004, **28**, 47-57.
3. A. Bueno-Lopez, *Appl. Catalysis B-Environ.*, 2014, **146**, 1-11.
4. (a) M. A. Centeno, T. R. Reina, S. Ivanova, O. H. Laguna and J. A. Odriozola, *Catalysts*, 2016, **6**, 30; (b) D. Carta, T. Montini, M. F. Casula, M. Monai, S. Bullita, P. Fornasiero and A. Corrias, *J. Mater. Chem. A*, 2017, **5**, 20024-20034.
5. K. H. Kim and S. K. Ihm, *J. Hazard. Mater.*, 2011, **186**, 16-34.
6. S. Yabe and T. Sato, *J. Solid State Chem.*, 2003, **171**, 7-11.
7. X. Q. Fu, C. Wang, H. C. Yu, Y. G. Wang and T. H. Wang, *Nanotechnology*, 2007, **18**, 145503.
8. K. M. Kumar, M. Mahendhiran, M. C. Diaz, N. Hernandez-Como, A. Hernandez-Eligio, G. Torres-Torres, S. Godavarthi and L. M. Gomez, *Mater. Lett.*, 2018, **214**, 15-19.
9. (a) W. C. Chueh, C. Falter, M. Abbott, D. Scipio, P. Furler, S. M. Haile and A. Steinfeld, *Science*, 2010, **330**, 1797-1801; (b) J. R. Scheffe, R. Jacot, G. R. Patzke and A. Steinfeld, *J. Phys. Chem. C*, 2013, **117**, 24104-24114.
10. X. D. Feng, D. C. Sayle, Z. L. Wang, M. S. Paras, B. Santora, A. C. Sutorik, T. X. T. Sayle, Y. Yang, Y. Ding, X. D. Wang and Y. S. Her, *Science*, 2006, **312**, 1504-1508.
11. (a) C. W. Sun, H. Li and L. Q. Chen, *Energy Environ. Sci.*, 2012, **5**, 8475-8505; (b) K. Wu, L. D. Sun and C. H. Yan, *Adv. Energy Mater.*, 2016, **6**, 46.
12. S. Urban, P. Dolcet, M. Moller, L. M. Che, P. J. Klar, I. Djerdj, S. Gross, B. M. Smarsly and H. Over, *Applied Catalysis B-Environmental*, 2016, **197**, 23-34.
13. R. Di Monte and J. Kašpar, *J. Mater. Chem.*, 2005, **15**, 633-648.
14. O. A. Marina, C. Bagger, S. Primdahl and M. Mogensen, *Solid State Ionics*, 1999, **123**, 199-208.
15. C. I. Hiley and R. I. Walton, *CrystEngComm*, 2016, **18**, 7656-7670.
16. G. S. Li, R. L. Smith and H. Inomata, *J. Am. Chem. Soc.*, 2001, **123**, 11091-11092.
17. P. Singh and M. S. Hegde, *J. Solid State Chem.*, 2008, **181**, 3248-3256.
18. K. Yamashita, K. V. Ramanujachary and M. Greenblatt, *Solid State Ionics*, 1995, **81**, 53-60.
19. M. C. Pearce and V. Thangadurai, *Asia Pac. J. Chem. Eng.*, 2009, **4**, 33-44.
20. S. S. Bhella, S. P. Shafi, F. Trobec, M. Bieringer and V. Thangadurai, *Inorg. Chem.*, 2010, **49**, 1699-1704.
21. G. F. Zhang, L. P. Li, G. S. Li, X. Q. Qiu and G. F. Yan, *Solid State Sciences*, 2009, **11**, 671-675.
22. (a) A. Rabenau, *Angew. Chem. - Int. Ed.*, 1985, **24**, 1026-1040; (b) S. Somiya and R. Roy, *Bull. Mater. Sci.*, 2000, **23**, 453-460; (c) R. E. Riman, W. L. Suchanek and M. M. Lencka, *Annal. Chim.-Sci. Mater.*, 2002, **27**, 15-36; (d) D. R. Modeshia and R. I. Walton, *Chem. Soc. Rev.*, 2010, **39**, 4303-4325; (e) G. Demazeau and A. Largeteau, *Z. Anorg. Allg. Chem.*, 2015, **641**, 159-163.
23. R. I. Walton, *Prog. Cryst. Growth Charact. Mater.*, 2011, **57**, 93-108.
24. C. I. Hiley, J. M. Fisher, D. Thompsett, R. J. Kashtiban, J. Sloan and R. I. Walton, *J. Mater. Chem. A*, 2015, **3**, 13072-13079.

25. K. Sardar, H. Y. Playford, R. J. Darton, E. R. Barney, A. C. Hannon, D. Tompsett, J. Fisher, R. J. Kashtiban, J. Sloan, S. Ramos, G. Cibin and R. I. Walton, *Chem. Mater.*, 2010, **22**, 6191-6201.
26. C. I. Hiley, H. Y. Playford, J. M. Fisher, N. C. Felix, D. Thompset, R. J. Kashtiban and R. I. Walton, *J. Am. Chem. Soc.*, 2018, **140**, 1588-1591.
27. R. D. Shannon, *Acta Crystallogr.*, 1976, **A32**, 751-767.
28. D. Horlait, L. Claparede, N. Clavier, S. Szenknect, N. Dacheux, J. Ravaux and R. Podor, *Inorg. Chem.*, 2011, **50**, 7150-7161.
29. (a) A. Mineshige, T. Taji, Y. Muroi, M. Kobune, S. Fujii, N. Nishi, M. Inaba and Z. Ogumi, *Solid State Ionics*, 2000, **135**, 481-485; (b) L. Li, F. Chen, J. Q. Lu and M. F. Luo, *J. Phys. Chem. A*, 2011, **115**, 7972-7977.
30. B. T. M. Willis, *Acta Crystallogr. Sect. A*, 1978, **34**, 88-90.
31. H. Mizoguchi, P. M. Woodward, S. H. Byeon and J. B. Parise, *J. Am. Chem. Soc.*, 2004, **126**, 3175-3184.
32. H. Watelet, G. Baud, J. P. Besse and R. Chevalier, *Mater. Res. Bull.*, 1982, **17**, 1155-1159.
33. C. Svensson, *Acta Crystallogr.*, 1974, **B30**, 458-461.
34. R. W. G. Wyckoff, in *Crystal Structures, Second edition*, Interscience Publishers, New York 1963, vol. 1, pp. 239-444.
35. M. Boaro, M. Vicario, C. de Leitenburg, G. Dolcetti and A. Trovarelli, *Catal. Today*, 2003, **77**, 407-417.
36. A. C. Larson and R. B. V. Dreele, *General Structure Analysis System (GSAS), Los Alamos National Laboratory Report*, 1994, **LAUR 86-748**.
37. B. H. Toby, *J. Appl. Cryst.*, 2001, **34**, 210-213.
38. A. J. Dent, G. Cibin, S. Ramos, A. D. Smith, S. M. Scott, L. Varandas, M. R. Pearson, N. A. Krumpa, C. P. Jones and P. E. Robbins, *Phys. Conf. Ser.*, 2009, **190**, 012039
39. B. Ravel and M. Newville, *J. Synchrotron Radiat.*, 2005, **12**, 537-541.